

www.acsaem.org Article

# Interface Tuning through the MoO<sub>3</sub> Additive in Al Paste to Enhance the Performance of Crystalline Silicon Solar Cells

Bo Zhang, Yongsheng Li, Yongji Chen, Haibiao Chen, Chen Zhu, Jian Liu, Yuan Lin, and Feng Pan  $^{\ast}$ 



Cite This: ACS Appl. Energy Mater. 2022, 5, 13254-13260



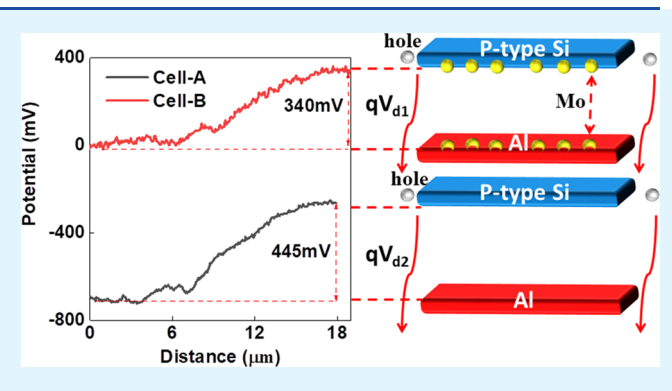
**ACCESS** I

III Metrics & More

Article Recommendations

SI Supporting Information

**ABSTRACT:** The efficiency of silicon solar cells is largely affected by the quality of the front and back metallic contacts. In this work, MoO<sub>3</sub> is added to the Al paste for the back contact of crystalline silicon solar cells. The MoO<sub>3</sub> additive lowers the series resistance of the solar cell from 4.1 to 3.5 m $\Omega$  and increases the photoelectric conversion efficiency from 19.26 to 19.54%. We identify that the thermite reaction between MoO<sub>3</sub> and Al takes place at about 800 °C and metallic Mo diffuses into the Al–Si solid layer, decreasing the barrier height between Al and Si and lowering the contact resistance. This work demonstrates an approach by optimizing the aluminum-back surface field (Al-BSF) in the back metallic contact of crystalline silicon solar cells to enhance the performance of the cell.



KEYWORDS: thermit reaction, back surface field, barrier height, contact resistance, series resistance

# 1. INTRODUCTION

As society calls for the expansion of utilization of clean energy, solar cells continue to be a major contributor to meet the demand. 1-3 The most critical benchmark for solar cells is the cell efficiency on which most research and development works are focused. Ohmic losses from the front and back metallic contacts of a cell take a very large proportion of all losses.<sup>4</sup> Therefore, there are continuously active research studies going on to minimize the back metallic loss. For the back metallic contact, there are mainly two strategies currently being undertaken. The first strategy is to optimize the back surface field (BSF) layer, which can improve cell efficiency via the enhanced field effect. It is known that the Al paste coating on the back surface of a cell can produce a BSF in silicon by thermal treatment.<sup>6</sup> In general, the formation of BSF follows the following four steps: (1) Al is deposited onto the back surface of silicon by screen printing; (2) alloying between Al and Si takes place when the cell is heated above the Al-Si eutectic temperature (about 577 °C); (3) epitaxial regrowth of the BSF when the cell starts to be cooled down; and (4) solidification of the Al-Si alloy when the eutectic temperature is reached. BSF is inside bulk silicon doped with a high content of Al, forming a p+/p structure, which can reduce the recombination of charge carriers and improve the electrical performance of the cells.<sup>8–11</sup> However, a high population of Al atoms can also become the recombination centers for the carriers. Recent works on the optimization of the BSF were focused on the glass frit, firing temperature, rate of the firing

processing, and the initial Al deposition technique. <sup>12–15</sup> In general, glass frit largely determines the adhesive property of Al on silicon as well as the sheet resistance, while the firing temperature and firing rate largely control the uniformity of the BSF, affecting the electrical performance of the cell. <sup>16,17</sup> Kim et al. studied the effects of Pb-free frit on the Al paste and discovered that the sheet resistance would decrease if the molar ratio between ZnO and B<sub>2</sub>O<sub>3</sub> increased. <sup>18</sup> Roberts et al. concluded that a uniform BSF can be obtained by increasing the alloying temperature and conducting rapid thermal processing. <sup>19,20</sup> Initial Al deposition has a significant impact on the thickness of BSF. Amick et al. identified the proportional relationship between the thicknesses of deposited Al and the resulting BSF, and they discovered that a thicker BSF achieved a longer minority carrier lifetime and a higher open-circuit voltage, leading to higher cell efficiency. <sup>14</sup>

The second strategy for optimizing the back contact is to decrease the contact barrier height between Al and Si directly. There are three common techniques to decrease the contact resistance between a metal and a semiconductor. The first method is to use a metal intermedia with a barrier height

Received: June 3, 2022 Accepted: October 5, 2022 Published: October 21, 2022





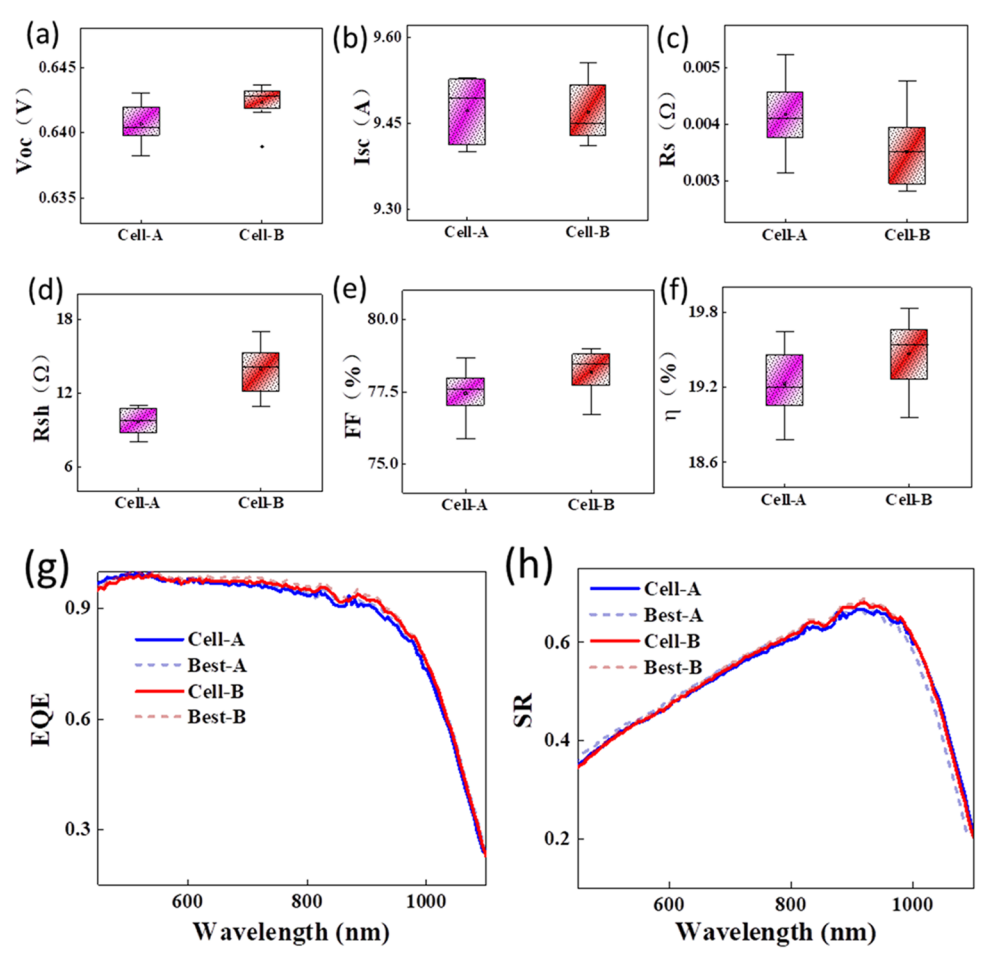


Figure 1. Statistics of the photovoltaic performance of Cell-A and Cell-B. (a) open-circuit voltage, (b) short circuit current, (c) series resistance, (d) shunt resistance, (e) fill factor, (f) power conversion efficiency, (g) external quantum efficiency, and (h) spectral response curves.

between the metal contact and the semiconductor. The second method is to deposit a thin layer of a material with a narrow band gap. The third method is to dope the semiconductor heavily. The third method is to dope the semiconductor heavily. Schroder et al. reviewed the metal contact resistance of solar cells and pointed out that metal Mo has a lower barrier height than Al in p-type silicon. It is a fact that aluminum can react with molybdenum trioxide in certain conditions. Schoenitz et al. performed kinetic analysis results of the reaction between aluminum and molybdenum trioxide. Here, we use MoO<sub>3</sub> as a sort of thermite for producing metallic Mo in situ while generating a significant amount of heat to form a thick BSF. Using this strategy, we are able to promote cell efficiency from 19.26 to 19.54%.

#### 2. EXPERIMENTAL SECTION

**2.1. Materials.** In our experiment, B<sub>2</sub>O<sub>3</sub>, ZnO, Al<sub>2</sub>O<sub>3</sub>, alcohol ester dodecyl, and butyl carbitol acetate were purchased from Aladdin. PbO, SiO<sub>2</sub>, and Sb<sub>2</sub>O<sub>3</sub> were purchased from Sinopharm Chemical Reagent Co., Ltd. Molybdenum trioxide was purchased from Shanghai Huayi (Group) Company. Ethyl cellulose N7 and ethyl cellulose N200 were purchased from Luzhou North Cellulose Co., Ltd. Acrylic resin was purchased from Shandong Lingyan Chemical Co., Ltd. Hydrogenated castor oil was purchased from Shandong Heju Electronic Technology Co., Ltd. Terpinol was purchased from Tianjin Baishi Chemical Co., Ltd. Al powder was purchased from HNJM Co., Ltd., China. Aluminum—silicon alloy powder was proprietary. All chemical reagents were of analytic grade. Monocrystalline (157 mm × 157 mm) and polycrystalline (156.75 mm ×

156.75 mm) silicon wafers were purchased from Wuxi Bokun Photovoltaic Technology Co., Ltd., China.

**2.2. Sample Preparation.** 2.2.1. Preparation of Glass. PbO,  $SiO_2$ ,  $B_2O_3$ , ZnO,  $Al_2O_3$ , and  $Sb_2O_3$  powders were thoroughly mixed in an alumina crucible, and the crucible was heated to  $1000\,^{\circ}$ C and held for half an hour in a furnace. The red-hot crucible was then taken out and quenched in water immediately. Finally, the glass was placed in a 60 °C oven to dry to obtain a glass block. The glass block was ground into a powder in an agate mortar with little ethanol. The powder was then wrapped in a piece of aluminum foil and dried in an oven. In this work, the basic recipe of the glass contained 14.97%  $B_2O_3$ , 5.03% ZnO, 1.99%  $Al_2O_3$ , 3.98%  $Sb_2O_3$ , 65.24% PbO, and 8.8%  $SiO_3$ .

2.2.2. Preparation of the Organic Carrier. Ethyl cellulose N7, ethyl cellulose N200, acrylic resin, hydrogenated castor oil, butyl carbitol acetate, alcohol ester dodecyl, and terpinol were thoroughly mixed in a mechanical agitator (T18 basic package, Hangzhou Qiwei Technology Co., Ltd., China) with a constant temperature water bath at 45 °C and stirred for 3 h at a stirring rate of 1500 rpm. The organic carrier of the aluminum paste was obtained. In this work, the basic recipe of the organic phase contained 1% ethyl cellulose N7, 2% ethyl cellulose N200, 1% acrylic resin, 1.5% hydrogenated castor oil, 25% butyl carbitol acetate, 25% alcohol ester, and 44.5% terpineol.

2.2.3. Preparation of Aluminum Paste. Aluminum powder, aluminum—silicon alloy powder, glass powder, molybdenum trioxide, organic carrier, and dispersant (BYK-110, Germany) were thoroughly mixed using a homogenizer (Z-200 V, ZYE, China). A multistage mixing procedure was set on the homogenizer. The mixture was first stirred at a speed of 800 r/min for 20 s, then at 1900 r/min for 70 s, and finally at 900 r/min for 20 s. This mixing procedure was repeated a total of three times, and the mixture was checked and manually

stirred between the homogenizer operations. The basic recipe of the aluminum paste in this work contained 25 wt % 2–3  $\mu$ m aluminum powder, 45 wt % 5–6  $\mu$ m aluminum powder, 5 wt % aluminum—silicon alloy powder, 1.5 wt % glass powder, 23 wt % organic carrier, and 0.5 wt % dispersant.

2.3. Material Characterization. The morphology of the materials was examined using a scanning electron microscope (SEM, ZEISS SUPRA-55) and the elements were analyzed by energy dispersive spectroscopy (EDS, OXFORD, X-MaxN TSR). The X-ray photoelectron spectra (XPS) were acquired using a Thermo Fisher ESCALAB 250Xi with an Al K $\alpha$  X-ray source, the sample was etched with Ar+ sputtering at a rate of about 0.5 nm/s, and all of the binding energies were calibrated with a C 1s signal at 284.8 eV. TGA measurements were conducted on a TGA/DSC 1 STARe system. The samples for the Kelvin probe force microscopy (KPFM) measurement were cut into 10 mm × 5 mm pieces by a laser. The samples were then polished by an Ar+ ion beam milling technique (Leica EM TIC 3X, Leica Microsystems GmbH, Germany) with an accelerating voltage of 6.5 kV and a beam current of 2.4 mA for 1 h, followed by Ar+ ion beam cutting with an accelerating voltage of 7.5 kV and a beam current of 2.8 mA for 2 h, and finally polished by Ar+ ion beams with an accelerating voltage of 7.0 kV and beam current of 2.6 mA for 0.5 h. The surface potential of the Al-Si interfaces was measured by an atomic force microscope (AFM, Dimension Icon, Bruker Co., Germany) using Pt/Ir-coated conducting tips (SCM-Pit) with a scan rate of 0.498 Hz. The I-V curves of photovoltaic devices were measured by a pulsed solar simulator (PSL SCD, BERGER Lichttechnik GmbH& Co.KG). The contact resistance is measured by a four-probe resistivity tester, testing in 1.0 mA and  $\rho$  mode (KDY-1, Guangzhou Kunde Technology Co., Ltd., China). The external quantum efficiency and spectral response curves of the cells were measured by a QE tester system (SCS1011, Zolix Instruments Co., Ltd., China).

## 3. RESULTS AND DISCUSSION

Al paste typically consists of aluminum powder (as shown in Figure S1), glass frit, and organic solvents.<sup>34–36</sup> In this work, the components were mixed and then stirred for a minute to form the blank Al paste which was labeled Paste A or P-A. By adding MoO<sub>3</sub> (as shown in Figure S1) to P-A, Paste B or P-B was produced. Monocrystalline silicon solar cells were fabricated using P-A and P-B following similar procedures and were labeled Cell-A and Cell-B, respectively. The performance of the crystalline silicon solar cells prepared for Cell-A and Cell-B is shown in Figure 1a-f. It can be compared with the statistical features of open-circuit voltage  $(V_{oc})$ , short circuit current  $(I_{sc})$ , series resistance  $(R_s)$ , shunt resistance  $(R_{\rm sh})$ , fill factor (FF), photoelectric conversion efficiency  $(\eta)$  of all of the cells. It can be clearly appreciated that the median values of  $R_s$  and Isc decrease, while  $V_{oc}$ ,  $R_{sh}$ , FF, and  $\eta$  increase for Cell-B in contrast to Cell-A. Table 1 summarizes the median value performance parameters for Cell-A and Cell-B (refer to Table S1 and Figure S3 for details). From the table, we can see that the series resistance of Cell-B is  $3.5 \times 10^{-3} \Omega_{\rm p}$ which is lower than that of Cell-A (4.1  $\times$  10<sup>-3</sup> $\Omega$ ). As a result,

Table 1. Test Results of Monocrystalline Solar Cells with and without the MoO<sub>3</sub> Additive in the Al Paste

sample	$V_{\text{oc}}^{a}$ (V)	$I_{\rm sc}^{b}$ (A)	$R_s^c(\Omega)$	$rac{R_{ m sh}^{}}{(\Omega 0)}$	FF <sup>e</sup> (%)	$\eta^f$ (%)
Cell-A	0.6404	9.494	$4.1 \times 10^{-3}$	9.77	77.60	19.26
Cell-B	0.6428	9.449	$3.5 \times 10^{-3}$	14.10	78.45	19.54

<sup>&</sup>lt;sup>a</sup>Open-circuit voltage  $(V_{oc})$ . <sup>b</sup>Short circuit current  $(I_{sc})$ . <sup>c</sup>Series resistance  $(R_s)$ . <sup>d</sup>Shunt resistance  $(R_{sh})$ . <sup>e</sup>Fill factor (FF). <sup>f</sup>Photoelectric conversion efficiency  $(\eta)$ .

the absolute value of the fill factor increases by about 0.85%, which leads to a noticeable improvement in efficiency (19.54 vs 19.26%). Using the same approach, we improved the performance of polycrystalline silicon solar cells, and the results are shown in Table S2 and Figure S4.

To understand the reason for the improvement in cell efficiency, further photoelectronic characterization is performed. The external quantum efficiency curves of the cells are depicted in Figure 1g. An increase in the long wavelength light absorption range ( $600-1000~\rm nm$ ) is observed for Cell-B in contrast to Cell-A, which indicates the improvement of the back surface of the cells. The spectral response curves of the cells are performed in the same way (see Figure 1h). All of the data of photoelectronic characterization prove the effectiveness of the MoO<sub>3</sub> additive to the Al paste of the solar cells.

All of the data above were measured under the standard conditions with AM  $1.5:100 \text{ mW/cm}^2$  illumination and room temperature at 25  $^{\circ}$ C.

To understand the internal mechanism of the fabricated cells, the schematic diagram of conventional crystalline silicon solar cells is depicted in Figure 2a. Then, scanning electron

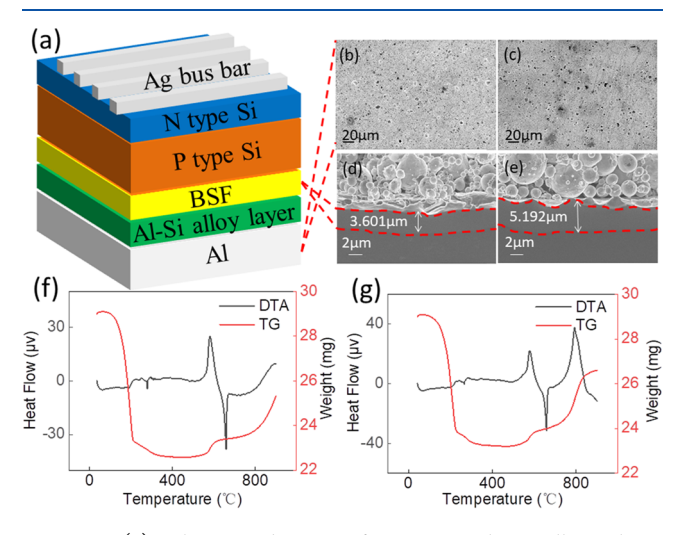


Figure 2. (a) Schematic diagram of conventional crystalline silicon solar cells. SEM images of (b, c) Al back surface and (d, e) BSF of Cell-A and Cell-B, respectively. DTA/TG curves of Al paste (f) P-A and (g) P-B in air with a heating rate of 10  $^{\circ}$ C/min from 25 to 900  $^{\circ}$ C.

microscopy (SEM) and differential thermal analysis (DTA) are employed. As shown in Figure 2g, there is a strong exothermic peak at about 800 °C in the DTA curve of Al paste with the MoO<sub>3</sub> additive when the reaction between MoO<sub>3</sub> and Al takes place.<sup>33</sup> In contrast, there is no exothermic peak in the DTA curve for the blank Al paste shown in Figure 2f. With the heat from the thermite reaction, Al particles melt extensively and big holes are formed, which are distributed on the back surface of the cells. The difference between the two cells can be seen in Figure 2b,c. Cell-B in Figure 2c containing more big holes is expected to have a higher sheet resistance than Cell-A, since the density of the Al paste layer is lower. Besides, the extensively melted Al particles on the surface of silicon result in a thicker BSF after being cooled down. According to the SEM images of BSF in Figure 2d,e, the BSF of Cell-B is thicker than that of Cell-A by about 1.6  $\mu$ m (5.2 vs 3.6  $\mu$ m).

To observe the distribution of the Mo element, we removed most of the Al layer covering the back surface using

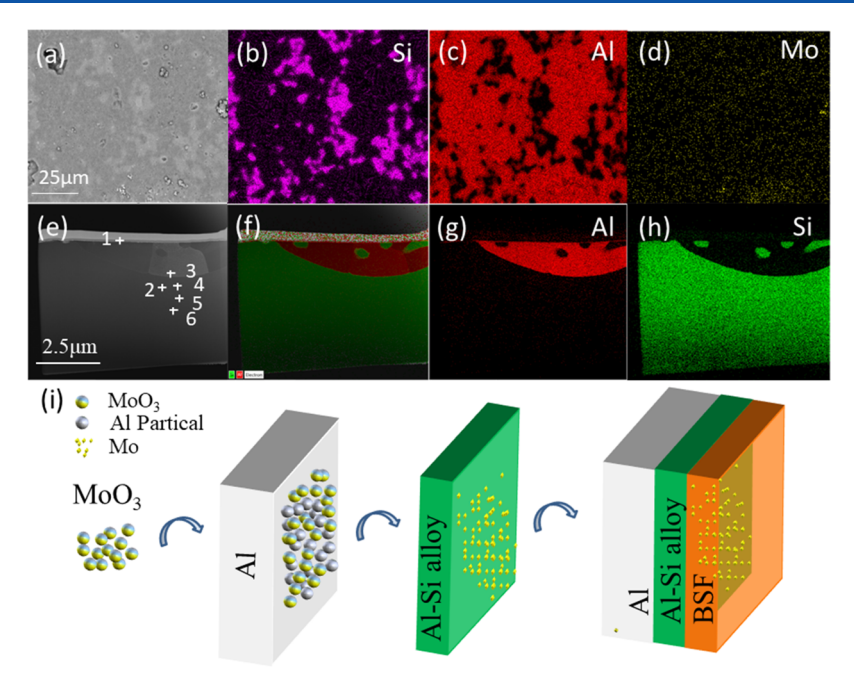


Figure 3. SEM and EDS of the Al–Si solid layer of Cell-B, which was etched for about 10 min with dilute hydrochloric acid and treated in 60 °C ultrasound cleaning for 1 h to remove most Al particles: (a) SEM and (b–d) EDS elemental mappings of elements Si, Al, and Mo, respectively. TEM and EDS images of the cross section of the Al–Si solid layer of Cell-B prepared with a focused ion beam: (e) TEM and sampling spots; (f) EDS elemental mapping; (g) EDS mapping of Al; and (h) EDS mapping of Si. (i) The schematic diagram of the diffusion process of the Mo element

hydrochloric acid and took SEM/EDS images of the back surface. The results are shown in Figure 3a-d. From the EDS elemental mapping of the Al-Si alloy layer, we can see the phase separation of Al and Si, which formed when the cell was cooled down after heating. Distribution of the Mo element across the surface of the Al-Si alloy layer was uniform, suggesting that Mo diffused into the Al-Si solid layer. To evaluate the distribution of the Mo element through the depth, the cell was cut across the Al-Si alloy layer and the cross section was observed under TEM, as shown in Figure 3e-h. According to the TEM and EDS images, there was an Al-Si alloy layer below the surface of the bulk Si. The contents of the elements at different depths from the surface were analyzed by EDS from six spots as marked in Figure 3e, and the results are shown in Table S3. The elemental analysis of the six spots showed that the Mo element tended to remain near the surface of the Al-Si alloy layer and the content was not so high (1.76 wt %). The schematic diagram of the migration process of the Mo element is shown in Figure 3i.

For further observing the valence states of molybdenum in the Al-Si alloy layer, the XPS spectra of the Al-Si solid layer etched for a variety of durations with Ar+ sputtering are shown in Figure 4a, and the XPS results of MoO<sub>3</sub> powder are shown in Figure 4b; the Mo 3d<sub>5/2</sub> peak is centered at 232.83 eV and the Mo 3d<sub>3/2</sub> peak is centered at 235.98 eV, both match the characteristic peaks of Mo<sup>+6</sup> according to previous reports.<sup>37,38</sup> As shown in Figure 4a, the XPS survey spectrum indicates the presence of metal Mo with characteristic peaks located at 228 and 231 eV, corresponding to Mo<sup>0</sup> 3d<sub>5/2</sub> and Mo<sup>0</sup> 3d<sub>3/2</sub>, respectively. 39,40 The XPS results confirmed that MoO<sub>3</sub> reacted with Al to produce metallic Mo. The metallic Mo atoms diffusing into the Al-Si solid layer could decrease the contact resistance between Al and Si.<sup>29</sup> As shown in Figure 4c, the contact resistance of Cell-B is almost only two-thirds that of Cell-A.

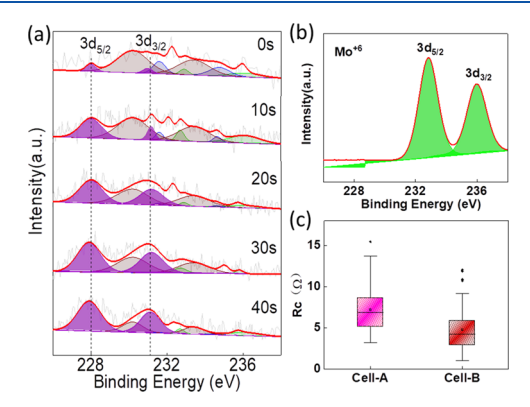


Figure 4. XPS of (a) the Al–Si solid layer of Cell-B etched 0, 10, 20, 30, and 40 s with  $Ar^+$  sputtering and (b) MoO<sub>3</sub> powder. (c) Contact resistance of Cell-A and Cell-B.

Moreover, for a better understanding of the mechanism of the reduced contact resistance, the surface potentials of the cross section for Cell-A and Cell-B were obtained by KPFM technology, and the results are shown in Figure 5. The surface potential between the tip and the sample was recorded as the tip scanned across the cross-sectional surface. The threedimensional surface potential profiles by KPFM are shown in Figure S5. Figure 5a,b shows the height profile images, which represent the surface morphology of the cross section. Figure 5c,d shows the surface potential maps generated in situ during the scan. From these images, we can easily identify regions with melted Al particles, Al-Si solid layer, and the silicon region containing BSF. Figure 5e,f shows the surface potential profile across the layers, from which we can see the overall surface potential step between the bulk Al and bulk Si regions in Cell-A and Cell-B. The surface potential steps between the bulk Al and bulk Si layer were 445 and 340 mV for Cell-A and

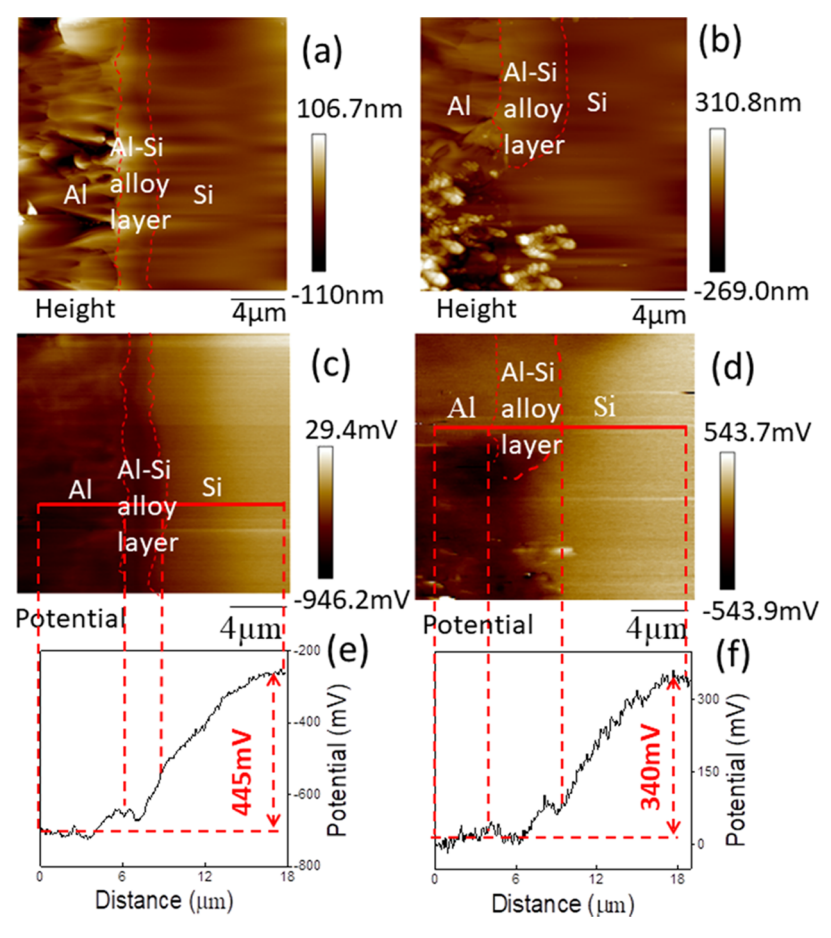
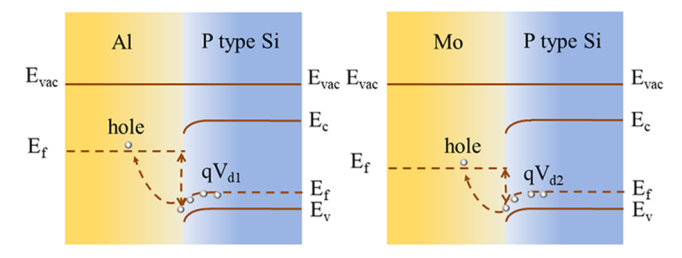


Figure 5. Topography images, surface potential images, and surface potential step images of (a, c, e) Cell-A and (b, d, f) Cell-B, respectively.

Cell-B, respectively. Obviously, the surface potential step is lower in Cell-B. The reaction between MoO<sub>3</sub> and Al produced metallic Mo, which diffused into the Al-Si solid layer and even into the BSF layer. Metallic Mo has a work function higher than Al in p-type Si, resulting in a lower barrier.<sup>29</sup> Therefore, when the solar cell generates electrons and holes under the light, holes can easily migrate through the low barrier area. For this reason, the contact resistance between Al and Si decreases when Mo is present. In fact, the series resistance of a cell includes Ag grid resistance, contact resistance between Ag and Si, Si bulk resistance, Al and Si contact resistance, and Al back surface sheet resistance. We use the same batch of Ag paste and silicon wafer to prepare the cells, so Ag grid resistance and Si bulk resistance can be considered the same for Cell-A and Cell-B. The Ag-Si contact resistance was quite similar in these two cells (as shown in Figure S2). The Al back surface sheet resistance of Cell-B was a little higher than that of Cell-A due to the porosity of the Al layer as observed previously. Therefore, it can be concluded that it was the reduction of the Al-Si contact resistance that resulted in the decrease of the series resistance.

The mechanism is shown in Figure 6. The work function of Mo is higher than that of Al, which leads to a lower barrier height between Mo and p-type silicon. Once metallic Mo diffuses into the Al–Si solid layer, leading to a decrease in the barrier height between Al and Si, the absolute photoelectric conversion efficiency increases by 0.28%.



**Figure 6.** Schematic diagram of the contact barrier height between p-type Si, Mo, and Al.

# 4. CONCLUSIONS

In summary, we developed a novel Al paste with the MoO<sub>3</sub> additive to enhance the performance of crystalline solar cells. MoO<sub>3</sub> reacted with Al particles to produce metallic Mo during thermal processing and release a lot of heat. Al particles melted extensively under the heat and led to the formation of a thick BSF area. The reaction produced metallic Mo atoms diffusing into the Al–Si solid layer and even the BSF area to lower the contact barrier between Al and Si. The decrease of the Al–Si contact resistance resulted in a lower series resistance than that of the cells without the MoO<sub>3</sub> additive. As a result, the absolute values of the fill factor and photoelectric conversion efficiency increased by 0.85 and 0.28%, respectively.

### ASSOCIATED CONTENT

# Supporting Information

The Supporting Information is available free of charge at https://pubs.acs.org/doi/10.1021/acsaem.2c01737.

SEM images of the starting materials for the Al paste: Al particles, Al–Si alloy powder, and MoO<sub>3</sub> powder; contact resistance between Ag and Si of Cell-A and Cell-B; detailed testing data of monocrystalline and polycrystalline silicon solar cells with a variety of MoO<sub>3</sub> doping content in the Al paste; and three-dimensional surface potential and topography images of KPFM for the cross section of Cell-A and Cell-B (PDF)

#### AUTHOR INFORMATION

#### **Corresponding Authors**

Jian Liu – School of Advanced Materials, Peking University, Shenzhen Graduate School, Shenzhen 518055, China; Email: 2101111317@stu.pku.edu.cn

Yuan Lin — Key Laboratory of Photochemistry, Institute of Chemistry, Chinese Academy of Sciences, Beijing 100190, China; ⊚ orcid.org/0000-0003-3410-3588; Email: linyuan@iccas.ac.cn

Feng Pan — School of Advanced Materials, Peking University, Shenzhen Graduate School, Shenzhen 518055, China; orcid.org/0000-0002-8216-1339; Email: panfeng@pkusz.edu.cn

#### **Authors**

Bo Zhang — School of Advanced Materials, Peking University, Shenzhen Graduate School, Shenzhen 518055, China

Yongsheng Li — School of Advanced Materials, Peking University, Shenzhen Graduate School, Shenzhen 518055, China

Yongji Chen — School of Advanced Materials, Peking University, Shenzhen Graduate School, Shenzhen 518055, China

Haibiao Chen — Institute of Marine Biomedicine, Shenzhen Polytechnic, Shenzhen 518055, China

Chen Zhu – School of Advanced Materials, Peking University, Shenzhen Graduate School, Shenzhen 518055, China

Complete contact information is available at: https://pubs.acs.org/10.1021/acsaem.2c01737

#### **Author Contributions**

B.Z. and Y.L. contributed equally to this work.

#### Notes

The authors declare no competing financial interest. The authors declare that they have no known competing financial interests or personal relationships that could have appeared to influence the work reported in this paper.

#### ACKNOWLEDGMENTS

The authors would like to thank the support of the Soft Science Research Project of Guangdong Province (No. 2017B030301013) and the Guangdong Innovative Team Program (No. 2013N080).

# REFERENCES

(1) Che, Q.; Yang, H.; Lu, L.; Wang, Y. A new environmental friendly silver front contact paste for crystalline silicon solar cells. *J. Alloys Compd.* **2013**, 549, 221–225.

- (2) Ma, Q.; Ma, S.; Bai, J.; Wang, H. Influence of lead-free glass frit in the front contact paste on the conversion efficiency of polycrystalline silicon solar cells. RSC Adv. 2017, 7, 47500–47506.
- (3) Li, H.; Tong, H.; Zhang, J.; Li, G.; Yang, Y.; Liu, C.; Li, H.; Yuan, X. Investigation on PbO-B<sub>2</sub>O<sub>3</sub>-SiO<sub>2</sub>-RxOy Glasses Applied in Noncontact Silver Paste for Crystalline Silicon Solar Cells. *J. Electron. Mater.* **2020**, *49*, 5422–5429.
- (4) Wang, H.; Ma, S.; Zhang, M.; Lan, F.; Wang, H.; Bai, J. Effects of screen printing and sintering processing of front side silver grid line on the electrical performances of multi-crystalline silicon solar cells. *J. Mater. Sci: Mater. Electron.* **2017**, 28, 11934–11949.
- (5) Joonwichien, S.; Moriya, M.; Utsunomiya, S.; Kida, Y.; Shirasawa, K.; Takato, H. Mechanism of Metallization-Induced Losses in the Rear-Side of Fully Screen-Printed p-type PERC Solar Cells. *IEEE J. Photovoltaics* **2020**, *10*, 407–416.
- (6) Fang, H.-C.; Liu, C.; Chung, H.; Huang, C. Effects of Fine Particle Content in Al Paste on Screen Printed Contact Formation and Solar Cell Performance. *J. Electrochem. Soc.* **2010**, *157*, 455–458.
- (7) Huster, F. In Investigation of the Alloying Process of Screen Printed Aluminum Pastes for the BSF Formation on Silicon Solar Cells, Proceedings of the 20th European Photovoltaic Solar Energy Conference; WIP Renewable Energies Barcelona, 2005; pp 1466–1469
- (8) Joonwichien, S.; Mochizuki, T.; Shirasawa, K.; Takato, H. Effects of different particle-sized Al pastes on rear local contact formation and cell performance in passivated emitter rear cells emitter rear cells. *Energy Procedia* **2017**, *124*, 412–417.
- (9) Mandelkorn, J.; Lamneck, J. H. Simplified fabrication of back surface electric field silicon cells and novel characteristics of such cells. *Solar Cells* **1990**, 29, 121–130.
- (10) Godlewski, M. P.; Baraona, C. R.; Brandhorst, H. W. Low-high junction theory applied to solar cells. *Sol. Cells* **1990**, *29*, 131–150.
- (11) Fossum, J. G. Physical operation of back-surface-field silicon solar cells. *IEEE Trans. Electron Devices* **1977**, 24, 322–325.
- (12) Narasimha, S.; Rohatgi, A.; Weeber, A. W. An Optimized rapid aluminum back surface field technique for silicon solar cells. *IEEE Trans. Electron Devices* **1999**, *46*, 1363–1370.
- (13) del Alamo, J.; Eguren, J.; Luque, A. Operating limits of Alalloyed High-low junctions for BSF solar cells. *Solid State Electron*. **1981**, 24, 415–420.
- (14) Amick, J. A.; Bottari, F. J.; Hanoka, J. The effect of aluminum thickness on solar cell performance. *J. Electrochem. Soc.* **1994**, *141*, 1577–1585.
- (15) Yi, J. H.; Koo, H. Y.; Kim, J. H.; Ko, Y. N.; Kang, Y. C.; Lee, H. M.; Yun, J. Y. Fine size Pb-based glass frit with spherical shape as the inorganic binder of Al electrode for Si solar cells. *J. Alloys Compd.* **2010**, 490, 488–492.
- (16) Saint-Cast, P.; Rüdiger, M.; Wolf, A.; Hofmann, M.; Rentsch, J.; Preu, R. Advanced analytical model for the effective recombination velocity of locally contacted surfaces. *J. Appl. Phys.* **2010**, *108*, No. 013705.
- (17) Saint-Cast, P. Passivation of Si Surfaces by PECVD Aluminum Oxide, Ph.D. Dissertation, Department of Physics, Universität of Konstanz: Konstanz, Germany, 2012.
- (18) Kim, B.-N.; Kim, D.-H.; Kim, H.-J.; Lee, H.; Chang, H.; Ryu, S.-S. Characterization and cell performance of Al paste with an inorganic binder of Bi<sub>2</sub>O<sub>3</sub>-B<sub>2</sub>O<sub>3</sub>-ZnO system in Si solar cells. *Curr. Nanosci.* **2014**, *10*, 66–69.
- (19) Roberts, F. M.; Wilkinson, L. G. The controlling factors in semiconductor large area alloying technology. *J. Mater. Sci.* **1968**, *3*, 110–119
- (20) Roberts, F. M.; Wilkinson, E. L. G. The effects of alloying material on regrowth-layer structure in silicon power devices. *J. Mater. Sci.* **1971**, *6*, 189–199.
- (21) Rhoderick, E. H. The physics of Schottky barriers. J. Phys. D: Appl. Phys. 1970, 3, 1153–1167.
- (22) Ebong, A.; Chen, N. In Metallization of Cystalline Silicon Solar cells: A Review, IEEE 2012 9th International Conference on High

- Capacity Optical Networks and Enabling Technologies (HONET): Istanbul, Turkey, 2012; pp 102–109.
- (23) Mead, C. A. "Physics of Interfaces," in Ohmic Contacts to Semiconductors; Schwartz, B., Ed.; Electrochem. SOC.: New York, 1969; pp 3–16.
- (24) Fall, C. J.; Binggeli, N.; Baldereschi, A. Anomaly in the anisotropy of the aluminum work function. *Phys. Rev. B.* **1998**, *58*, R7544–R7547.
- (25) Cheng, S.; Tan, C. M.; Deng, T.; He, F.; Zhang, S.; Su, H. In *Investigation of Work Function and Surface Energy of Aluminum: An Ab-Initio Study*, 2013 IEEE 5th International Nanoelectronics Conference (INEC); IEEE, 2013; pp 473–475.
- (26) Berge, S.; Gartland, P. O.; Slagsvold, B. J. Photoelectric work function of a molybdenum single crystal for the (100), (110), (111), (112), (114), and (332) faces. *Surf. Sci.* **1974**, *43*, 275–292.
- (27) Weber, A. H.; Zepf, T. H. Photoelectric and thermionic schottky deviations for molybdenum single crystals. *Surf. Sci.* **1969**, 14, 247–265.
- (28) Bzaszczyszyn, M. Work function of adsorption systems potassium on tantalum. Surf. Sci. 1976, 59, 533-540.
- (29) Schroder, D. K.; Meier, D. L. Solar Cell Contact Resistance-A Review. *IEEE Trans. Electron Devices* **1984**, *31*, 637–647.
- (30) Xue, Y.; Ren, X.; Xie, R.; Shi, C.; Liu, L.; Zhang, Y. Ignition performance of nano Al-MoO $_3$ . Chin. J. Energ. Mater. **2010**, 18, 674–676.
- (31) Umbrajkar, S. M.; Seshadri, S.; Schoenitz, M.; Hoffmann, V. K.; Dreizin, E. L. Aluminum-Rich Al-MoO $_3$  Nanocomposite Powders Prepared by Arrested Reactive Milling. *J. Propul. Power* **2008**, 24, 192–198.
- (32) Seo, H.-S.; Kim, J.-K.; Kim, J.-W.; Kim, H.-S.; Koo, K.-K. Thermal behavior of Al/MoO<sub>3</sub> xerogel nanocomposites. *J. Ind. Eng. Chem.* **2014**, *20*, 189–193.
- (33) Schoenitz, M.; Umbrajkar, S. M.; Dreizin, E. L. Kinetic Analysis of Thermite Reactions in Al-MoO3 Nanocomposites. *J. Propul. Power* **2007**, 23, 683–687.
- (34) Sopian, K.; Amin, N.; Asim, N.; Zaidi, S. H. Plasma Implantation for Emitter and Localized Back Surface Field (BSF) Formation in Silicon Solar Cells. *J. Sci. Res.* **2008**, *24*, 365–372.
- (35) Lin, C. H.; Tsai, S. Y.; Hsu, S. P.; Hsieh, M. H. Investigation of Ag-bulk/glassy-phase/Si heterostructures of printed Ag contacts on crystalline Si solar cells. *Sol. Energy Mater. Sol. Cells* **2008**, 92, 1011–1015.
- (36) Kim, S.; Sridharan, S.; Khadilkar, C.; Shaikh, A. In *Aluminum Pastes (Lead-Free/Low-Bow) for Thin Wafers*, Conference Record of the Thirty-first IEEE Photovoltaic Specialists Conference; IEEE, 2005; pp 1100–1102.
- (37) Li, H.; Chen, J.; Cui, M.; Cai, G.; Eh, A. L.-S.; Lee, P.; Wang, H.; Zhang, Q.; Li, Y. Spray coated ultrathin films from aqueous tungsten molybdenum oxide nanoparticle ink for high contrast electrochromic applications. *J. Mater. Chem. C.* **2016**, *4*, 33–38.
- (38) Bica de Moraes, M. A.; Trasferetti, B. C.; Rouxinol, F. P.; Landers, R.; et al. Molybdenum Oxide Thin Films Obtained by the Hot-Filament Metal Oxide Deposition Technique. *Chem. Mater.* **2004**, *16*, 513–520.
- (39) Song, Z.; Cai, T.; Chang, Z.; Liu, G.; Rodriguez, J. A.; Hrbek, J. Molecular Level Study of the Formation and the Spread of MoO<sub>3</sub> on Au (111) by Scanning Tunneling Microscopy and X-ray Photoelectron Spectroscopy. *J. Am. Chem. Soc.* **2003**, *125*, 8059–8066.
- (40) Wagner, C. D.; Riggs, W. M.; Davis, L. E.; Moulder, J. F.; Muilenberg, G. E. *Handbook of X-rays Photoelectron Spectroscopy*; Perkin-Elmer: Minnesota, 1978; p 104.

